HHS Public Access

Author manuscript

Magn Reson Med. Author manuscript; available in PMC 2016 June 01.

Published in final edited form as:

Magn Reson Med. 2015 June ; 73(6): 2363–2375. doi:10.1002/mrm.25335.

A 31-Channel MR Brain Array Coil Compatible with Positron Emission Tomography

Christin Y. Sander[a,b], **Boris Keil**[a], **Daniel B. Chonde**[a], **Bruce R. Rosen**[a,c,d], **Ciprian Catana**[a], and **Lawrence L. Wald**[a,c]

[a]Athinoula A. Martinos Center for Biomedical Imaging, Massachusetts General Hospital, Harvard Medical School, Charlestown, MA, United States

[b]Electrical Engineering and Computer Science, Massachusetts Institute of Technology, Cambridge, MA, United States

[c]Health Sciences and Technology, Harvard-MIT, Cambridge, MA, United States

[d]Department of Meridian & Acupuncture, Collaborating Center for Traditional Medicine, East-West Medical Research Institute and School of Korean Medicine, Kyung Hee University, Seoul, Republic of Korea

Abstract

Purpose—Simultaneous acquisition of MR and PET images requires the placement of the MR detection coil inside the PET detector ring where it absorbs and scatters photons. This constraint is the principal barrier to achieving optimum sensitivity on each modality. Here, we present a 31-channel PET-compatible brain array coil with reduced attenuation but improved MR sensitivity.

Methods—A series of component tests were performed to identify tradeoffs between PET and MR performance. Aspects studied include the remote positioning of preamplifiers, coax size, coil trace size/material, and plastic housing. We then maximized PET performance at minimal cost to MR sensitivity. The coil was evaluated for MR performance (SNR, g-factor) and PET attenuation.

Results—The coil design showed an improvement in attenuation by 190% (average) compared to conventional 32-channel arrays, and no loss in MR SNR. Moreover, the 31-channel coil displayed an SNR improvement of 230% (cortical ROI) compared to a PET-optimized 8-channel array with similar attenuation properties. Implementing attenuation correction of the 31-channel array successfully removed PET artifacts, which were comparable to those of the 8-channel array.

Conclusion—The design of the 31-channel PET-compatible coil enables higher sensitivity for PET/MR imaging, paving the way for novel applications in this hybrid-imaging domain.

Keywords

simultaneous PET/MR; integrated PET/MR; multi-channel brain array; RF coil attenuation; PET-optimized coil

Corresponding author: Christin Y. Sander, csander@mit.edu, Phone: 617 724 1839, Athinoula A. Martinos Center for Biomedical Imaging, Massachusetts General Hospital, 149 13th Street, Suite 2301, Charlestown, MA 02129, United States, Electrical Engineering, Massachusetts Institute of Technology, 77 Massachusetts Avenue, Bldg. 36-792, Cambridge, MA 02139, United States.

Introduction

Imaging technology for simultaneous Magnetic Resonance Imaging (MRI) and Positron Emission Tomography (PET) has been developed in the last decade for small-animal imaging (1) and more recently for human imaging applications (2). Integrated simultaneous PET and MRI allow a unique combination of morphology and function by combining high resolution anatomical MR, hemodynamic changes from functional MRI (fMRI), and specific functional molecular imaging from PET (3, 4). The potential and the growing interest for studies with simultaneous positron emission tomography/magnetic resonance (PET/MR) imaging (5) calls for advanced detection capabilities with integrated PET/MR scanners, including new radiofrequency (RF) coils that improve sensitivity and parallel imaging.

From the MR perspective, large coil arrays for highly parallel imaging with MR-only scanners have demonstrated increased image sensitivity and acquisition speed compared to single-channel coils (6, 7, 8). The development of parallel imaging has allowed accelerated image acquisition and advanced reconstruction techniques with array coils (9, 10). For imaging of the brain, multi-channel array coils with up to 32 channels (or 64 channels for head/neck) are commercially available and arrays with higher numbers of channels have been demonstrated (11). However, the molar sensitivity in the functional/molecular domains of MRI is still orders of magnitude lower compared to PET (1) and hence there is a continuing drive for higher sensitivity.

In PET/MR imaging, the RF coils for the MR signal detection are located within the PET field-of-view (FOV) and thus degrade PET image quality through additional attenuation and scatter. These phenomena result in decreased sensitivity in PET images (i.e. increased image noise or longer PET acquisition times to make up for the counts absorbed by the MR array) as well as in the introduction of artifacts if the coil attenuation is not accounted for (12). Since standard RF coils are not PET-optimized and contain highly attenuating materials at non-uniformly distributed points in the PET FOV, artifacts on PET images due to RF coils can be a severe problem, especially for multi-channel arrays. While it is necessary to correct for the attenuation of the RF coil sitting inside the PET FOV, such corrections can be challenging and artifacts cannot always be fully removed (13–16). Thus, it is crucial to minimize the attenuation of photons for best PET image quality.

The design and development of multi-channel array coils for the use in an integrated PET/MR system poses new challenges and requires a different design approach compared to conventional MR arrays (14). For brain imaging with simultaneous PET/MR systems, MR arrays with a maximum of 12 channels are currently available. Higher number of channels would increase MR image quality, but would also be expected to increase the attenuation of 511 keV PET photons. Hence, it is especially important for the construction of highly parallel arrays to adopt a targeted design approach that takes into account PET compatibility while maximizing the MR detection capability. Other considerations are important, such as highly constrained space due to the small geometry of some current generation PET/MR brain scanners.

In this paper, we present the design and performance of a 31-channel PET-compatible MR brain array coil for simultaneous PET/MR. Detailed design considerations for the challenges with integrated PET/MR systems are addressed. These include choices for electrical components and their arrangement within the PET scanner bore. According to these criteria, the array coil is designed in a sparse configuration of 511 keV absorptive materials and aims to optimize the arrangement of components, such as preamplifiers and cables. The performance of the coil is evaluated according to MR SNR and parallel imaging measures as well as the principal factors for sensitive and artifact-free PET images: attenuation at 511 keV and the performance of coil attenuation corrections.

Methods

Existing hardware components

The PET-compatible array coil was designed for a prototype simultaneous PET/MR scanner, composed of a 3 Tesla MRI scanner (MAGNETOM Trio, Tim system, Siemens AG, Healthcare Sector, Erlangen Germany) and a PET camera insert (BrainPET, Siemens AG, Healthcare Sector, Erlangen Germany) with magnetic field insensitive avalanche photodiodes as scintillation detectors. The standard coil provided for this scanner includes an 8-channel receive coil with a local circularly polarized birdcage transmit coil. The PET camera has inner and outer physical diameters of 35 and 60 cm respectively, with an axial PET FOV of 19.25 cm.

PET compatibility of coil design

The 31-channel coil was designed to minimize the attenuation and scatter of 511 keV photons and thus be PET-compatible. To assess the attenuation properties of coil components inside the PET FOV, CT scans of components were taken with a clinical CT scanner (Discovery STE, GE Healthcare, Chalfont St. Giles, UK). Hounsfield units (HU) from the CT scans were converted into linear attenuation coefficients at 511 keV PET energies via a bilinear transformation (24). Additionally, estimates of attenuation at 511 keV were calculated with the Beer-Lambert law, using documented values of linear attenuation coefficients (28).

Coil components were evaluated for their tradeoff between PET compatibility (attenuation properties), MR SNR properties and necessary practical considerations (e.g. mechanical stability). In Figure 1, a range of coil components and their properties are displayed. Various wire thicknesses (16 to 24 awg), and different materials (copper and aluminum) for conducting loops were investigated. Also, two types of coaxial cables with a diameter of 2.2 and 1.2 mm were compared. The impact of using longer coaxial cables to connect conducting loops and preamplifiers was assessed in order to consider the removal of the preamplifiers from the PET FOV. Finally, the attenuation of preamplifiers on circuit boards (Figure 1, column 3) and plastic housing samples with various thicknesses (2 mm to 12 mm) was measured.

To test the performance of components for MR imaging, we built single test loop coils for each coil component option and compared SNR performance. Additionally, silver-based

conductive epoxy was evaluated as an alternative to solder for connecting components because of its lower density that would limit attenuation. The final design choice was based on maximizing sensitivity for the two imaging modalities, while minimizing loss of signal.

Array coil design

The 31-channel receive (Rx) array coil was designed to be placed inside a commercially available local head transmit coil of the BrainPET camera (Figure 2). The Rx helmet former was designed with a 3D CAD program (Sketchup, Google, Mountain View, CA, USA). As the transmit (Tx) coil accommodates space for a cylinder with a diameter of 28.5 cm, the Rx was designed with a maximum diameter of 28.3 cm to achieve a tight fit into the Tx. Since the Tx coil consists of a splitable housing, we incorporated a split coil former into the design of the Rx for easy patient access (Figure 2c).

The overall shape and size of the helmet curvature was based on an aligned head MRI and scaled to the 95th percentile of male head circumferences. In order not to obstruct the subject's view and to be able to utilize visual stimulus equipment, cutouts for the eyes were incorporated. The shape of the posterior housing follows natural head contours to support the patient's neck and improve sensitivity towards the occipital lobe and cerebellum. The entire coil was closed with a thin plastic housing to provide coverage of electronics. The final design of the array coil was printed from polycarbonate plastic on a three-dimensional printer (Fortus 400mc, Stratasys, Eden Prairie, MN, USA).

Coil construction

The layout of the array with overlapped circular coil elements was established with a hexagonal and pentagonal tiling pattern (6). The pattern was engraved onto the helmet with the CAD program, in addition to standoffs for preamplifiers and cable trap holders. The coil loop diameters were derived from the size of the pentagon or hexagon tiles, resulting in a diameter of 75 mm and 90 mm respectively. The array was designed to consist of 31 loop elements, plus 1 volume receive channel associated with the Tx. Since the scanner has 32 available receive channels in total, this design used the maximum number of channels possible. The anterior coil segment comprised 15 loop coils, where 13 loops correspond to hexagons and 2 loops to pentagon positions. In the posterior segment, we incorporated 16 loops (13 at hexagon and 3 at pentagons locations).

Based on our component evaluation, we used an 18-awg thick tin-plated copper wire (Figure 1). Bridges were bent into the wires to allow conductor crossings without contact. Each loop was split into three segments of equal lengths, interleaved with components mounted on small FR4 circuit boards (Figure 3). A split into three wire segments (instead of six segments that may be used for coils of this size) reduces the total number of components on the coil, further minimizing attenuation. The circuit boards were produced with a rapid prototyping circuit router (T-Tech-7000, T-Tech, Inc., Norcross, GA, USA) and their size was held as small as possible. A variable capacitor C_1 was used for fine-tuning the loop resonance to the resonant frequency (123.25 MHz) of the scanner. A fuse F (570 mA rating) served as passive protection against potentially large currents induced by the transmit system. The array coil was geometrically decoupled using an overlapped coil element

layout. Adjacent loops between the anterior/posterior housing were overlapped with a mechanical rim system, with loops in the anterior segment bent over the housing's rim structure to achieve critical overlap with its nearest neighbors from the posterior housing segment (Figure 1c). In order to utilize a sparse housing structure around the eyes, the two eye loops were decoupled by a shared impedance.

Each coil element's output circuitry comprised a capacitive voltage divider (C_3, C_4) to match the loop impedance to the preamplifier as shown in Figure 3. An active detuning circuit across the matching capacitor C_4 was composed of a variable inductor L_1 (hand-wound) and a PIN diode D (Macom, MA4P4002B-402, Lowell, MA, USA). During transmit, the PIN diode is forward biased and the activated parallel LC_4 circuit provides a high impedance within the coil loop. Prior to mounting the output circuitry to the coil helmet, these traps were pre-tuned to the Larmor frequency using a small sniffer probe for S_{11} monitoring. After populating the array coil, the active detuning traps were fine-tuned using a double-probe slightly coupled into the loop under test and adjusted via a S_{21} measurement.

Preamplifier decoupling was achieved by transforming the low impedance of the preamplifier to a short across the PIN diode using a $\lambda/2$ phase shift. This activates the detuning trap to transform a serial high impedance into the coil loop. Thus, current flow is minimized and inductive coupling to neighboring coils is reduced. Since all preamplifiers are placed outside the PET FOV, the distance of the coil element and preamplifiers varies from 10 mm to 100 mm. We compensated for these distances with a pi phase shifter (Figure 3) located between coaxial cable and preamplifier, while maintaining the desired $\lambda/2$ phase shift needed to transform the preamplifier input impedance to a short across the diode.

Due to space constraints and preamplifier placement outside the PET FOV, we placed 23 preamplifiers at the superior end of the coil, with the remaining eight placed at the inferior end of the helmet. We aligned all preamplifiers in z-direction to the magnetic field B_0 to prevent Hall effect issues on the drain current of the Field Effect Transistor (23). Output cables from the preamplifiers were bundled together with eight outputs into one cable trap each to prevent common mode currents and interference during RF transmit.

During the design layout, special attention was paid to prevent output cables from passing through the PET FOV. Three cable outputs with eight channels each were positioned to leave the coil towards the back of the scanner. One of these plugs also included the transmission lines for receive and transmit paths for the local birdcage Tx. The eight channels with preamplifiers positioned at the inferior end of the coil were bundled into one plug exiting at the neck end of the housing. These plug arrangements allowed a complete elimination of output cables from the PET FOV (see Figure S1 in Supplementary Material).

Coil bench tests

Bench testing during construction was carried out with a custom-made coil-plug simulator that provides 10 V for the preamplifiers and has the ability to manually apply bias current (100 mA) to each PIN diode on the array elements. Bench measurements verified element tuning, active detuning, nearest-neighbor coupling and preamplifier decoupling for each coil

element. The ratio of unloaded-to-loaded quality factor (Q_U/Q_L) was measured for each coil element size. The Q_U/Q_L-ratios were obtained for a loop with no coaxial cable or preamplifier and were tested with the loops external to the array assembly.

Initially, all loops but the element under test were detuned with a DC bias. The S_{21} measure of a double-probe was used to adjust active detuning by maximizing the difference between S_{21} measures in the tuned and unturned state. Geometrical decoupling of adjacent loop pairs was carried out by a direct S_{21} measurement, in which coaxial cables were connected from the each preamplifier input socket of two adjacent loops to the network analyzer while all other elements were kept actively detuned. The overlap percentage of each coil pair was then adjusted empirically by bending the overlapped part of the wire of each loop to achieve isolation between −13 dB and −18 dB.

We measured preamplifier decoupling of a given loop with all other loops detuned. Preamplifier decoupling was measured as the change in S_{21}, while the coil output coaxial cable was terminated with two different match conditions (30): first, with a powered preamplifier (low impedance termination) and second, with a power matched source impedance (i.e. 50 Ω). For each loop in turn, the bias voltage was turned off to measure preamplifier decoupling.

For the scanner setup with the BrainPET insert, a commercially available PET-optimized local transmit coil (Siemens AG, Healthcare Sector, Erlangen, Germany) encloses the 31-channel Rx. Due to the close proximity of the two coils, we observed both a shift and a split in resonant frequency for the transmit coil when the detuned array coil was placed inside the birdcage. This was attributed to residual coupling between the two coils and we had to carefully retune and restore circularly polarized symmetry of the transmit coil. This would be a lesser issue in whole body PET/MR applications, where the body Tx is located further away from the Rx array.

MRI data acquisition and analysis

Images were acquired with a head-shaped phantom filled with physiological saline and gadolinium. SNR measurements were taken with proton density weighted gradient echo images (repetition time TR = 30 ms, echo time TE = 6 ms, flip angle FA = 30°, slice thickness = 7 mm, matrix = 192 × 192 pixels, FOV_{MR} = 235 × 235 mm^2, bandwidth BW = 200 Hz/pixel). SNR maps were computed with the noise covariance weighted root sum-of-squares from individual channel images (31). In order to assess noise amplification in SENSE reconstructions, g-factor maps (9) were calculated from the complex coil sensitivity maps and the noise correlation matrix using the same imaging sequence but with an adjusted FOV (210 × 210 mm^2). SNR and g-factor measures were compared to those from the 8-channel head coil dedicated for the PET/MR system. Additionally, comparisons were made to a commercially available 32-channel head coil in the same MR scanner but with the PET insert taken out and a body coil used for transmit.

Human PET/MR images were acquired for comparisons between the 8-channel and 31-channel coil. T1-weighted MR images were acquired with the multiecho MPRAGE

sequence (MEMPRAGE, (32)) at 1mm isotropic resolution and with TR = 2530 ms, TE = 1.64 ms, TI = 1200 ms, FA = 7° and BW = 651 Hz/pixel.

CT data acquisition and processing

CT scans of coil components and the final coil design were acquired with a clinical CT scanner (GE Discovery STE). Images were acquired in helical scanning mode with x-ray tube current-time-product = 580 mAs, maximum voltage kVp = 140 kV, spiral pitch factor = 0.98, slice thickness = 0.625 mm, matrix = 512 × 512 pixels. The FOV was adjusted to the size of the coil in each case.

To evaluate the attenuation of each coil, CT scans were processed for an estimate of the coil attenuation at 511 keV in sinogram space: First, CT images in Hounsfield Units (HU) were converted to an attenuation map in units of linear attenuation coefficients at 511 keV (in cm^{-1}) by a bilinear transformation (24). The Radon transform was then applied to bring the data into sinogram space of angle versus radius. A sinogram of attenuation correction factors (ACF) was then obtained by evaluating the exponential of the Radon transform result.

Derivation of the 31-channel coil attenuation map

An attenuation map of the coil was created from the CT images of the 31-channel array. Streak artifacts on the CT images due to highly attenuating metal components were removed manually before extrapolating to 511 keV energies. In order to obtain an accurate positioning of the attenuation map in the PET FOV, four fillable fiducial markers were placed at fixed locations on the coil. The markers were filled with contrast agent during the CT scan and [^{18}F]-solution for a PET scan. The fiducial markers from the CT were then registered to the PET to place the coil attenuation map in an accurate position in the PET FOV. Attenuation maps were blurred to match PET resolution using a 3 mm FWHM Gaussian kernel and noise reduction.

PET data acquisition and reconstruction

To test the CT-derived coil attenuation map, PET data were acquired with an [^{18}F]-solution filled phantom (~0.4 mCi in 1.9 L). The phantom was placed in a fixed position on the patient bed and scanned in three configurations in the following order: with (i) the 31-channel or (ii) the 8-channel coil in place, or (iii) without any coil in the PET FOV. To compensate for the reduced activity over time (for the 2nd and 3rd scans), scan durations were adjusted to match the same activity levels in each scan: (i) 12.6 min, (ii) 17.3 min and (iii) 20 min for the three configurations above. An attenuation map of the phantom was derived from an initial PET image that was first reconstructed without attenuation correction and then thresholded to create a binary mask. The linear attenuation coefficient corresponding to water (0.096 cm^{-1}) was assigned to all the voxels inside the mask. The same attenuation map was used for all reconstructions, co-registered to each initial PET image to account for small changes in position. PET data were reconstructed with a standard 3D ordinary Poisson expectation maximization algorithm (OP-EM, 32 iterations), using both prompt and variance-reduced random coincidence events (25) as well as normalization, scatter (26) and attenuation sinograms. The reconstructed volume consisted of a 256 × 256 × 153 matrix with isotropic voxel size of 1.25 mm. Final images were smoothed with a 3 mm

FWHM Gaussian kernel (8 mm for the computation of difference images). Images were reconstructed either including or ignoring the coil attenuation maps. Normalized difference images were computed as the difference in phantom images taken with the coil and the reference image (no coil in PET FOV) and were divided by the reference image and masked to compute relative change values inside the phantom.

Human PET (and MR) data was acquired at 73 and 116 min after injection of [^{18}F]FDG (5 mCi injected activity), first with the 31-channel and then with the 8-channel coil in place. To match the total activity (and thus SNR) for the two scans, the duration of the PET scan was adjusted to 15 min and 20 min for the 31-channel and 8-channel coil acquisitions, respectively. A pseudo-CT attenuation map of the head was derived from an anatomical MEMPRAGE scan (see *MRI data acquisition and analysis*) and used for attenuation correction of the head (33). Otherwise, PET data were reconstructed as described above (26). All studies were carried out in compliance with the Institutional Review Board at Massachusetts General Hospital.

Results

Coil component evaluation

The material PET/MR performance trade-offs and final design choices for the 31-channel PET/MR coil are summarized in Figure 1. For the loop wire choices (Figure 1, column 1), SNR values decreased with wire diameter. Loops built with conductive epoxy showed a lower quality factor and connections were not strong enough for a stable array, so that standard solder was used in all cases. Relative to a standard 16 awg wire, the 18 awg and 24 awg wire showed a 6.2% and 22% reduction in SNR respectively. The aluminum foil loop showed a 25% decrease in SNR. Calculations from the Beer-Lambert law showed an estimated maximum beam attenuation of 9% from a 16 awg wire, 7% from an 18 awg wire and 3% from a 24 awg wire. Based on these measurements, the 18 awg wire was chosen for the final design as a compromise to preserve SNR and limit attenuation of 511 keV photons.

The second column in Figure 1 compares the performance of two coaxial cables of different thickness that connect the coil and preamplifier. The graph illustrates the SNR performance as a function of depth into the phantom. Both coaxial cables showed similar SNR performance, such that the thinner 1.2 mm silver coaxial cable was chosen for the final design.

With the CT scan and attenuation map (Figure 1, column 3), we showed that the preamplifiers are the most attenuating components of the coil. If the preamplifier is moved away from the PET FOV, i.e. the distance between loop and preamplifier is increased from 40 mm to 100 mm, an average loss of 8% in SNR is shown. This small loss was deemed acceptable in light of the reduced attenuation from preamplifiers. A distance of 100 mm was the largest length of coaxial cable needed for all preamplifiers to be placed outside the PET FOV.

The plastic housing (Figure 1, column 4) was chosen to have minimal thickness wherever possible, taking into account mechanical stability of the housing. The shell was thus chosen

to have a thickness of less than 2.7 mm on a flat surface, which corresponds to an attenuation of 3% according to the Beer-Lambert law.

MR performance of array coil

The single loop unloaded/loaded quality factor for a 90 mm loop was measured as 230/45, (≈ 5.1 ratio) for a single coil loop. In Figure 4, the noise correlation matrix of the 31-channel PET/MR coil is shown in comparison with the 8-channel PET/MR and the 31-channel MR-only phased array coil. The noise correlation ranges from 1% to 65% and averages with 21.4%, excluding the diagonal elements. Geometric decoupling on the bench achieved an average attenuation of −15.2 dB, with minimum attenuation of −13.0 dB and maximum of −22.2 dB. Preamplifier decoupling allowed for an additional −25 dB attenuation. To compare, the 8-channel PET/MR and 32-channel MR-only array achieve an average noise correlation of 11.8% (max: 20%, min: 1%) and 12.4% (max: 44%, min: 0.1%) respectively.

The MR SNR maps of a representative sagittal and axial slice for each of the three coils are shown in Figure 5. The gain in SNR, relative to the 8-channel array, was calculated for regions of interests with an area of 18×18 mm^2 placed at locations (a) to (f) (Figure 5). The highest SNR values of the 31-channel array are found at the periphery, close to the coil elements. In the sagittal slice, SNR gains were 2.3 (a, frontal region), 1.6 (b, center) and 1.7 (c, posterior region). In the axial slice, SNR gains were 2.2 (d, anterior region), 2.1 (f, posterior region) and 1.8 (e, center).

Figure 6 (*top*) shows inverted g-factor maps for an axial slice (same slice position as for the SNR maps) for the three coils in comparison. Four one-dimensional accelerations in the anterior-posterior direction with acceleration factor R = 2 to R = 5 and four two-dimensional accelerations with additional right-left directions are compared for the three coils. For the 8-channel array, the g-factor increases rapidly for R>2, translating into increased image noise amplification, whereas the 31-channel array consistently shows an overall lower g-factor. Comparison to the 32-channel MR-only array demonstrates that the 31-channel PET-optimized array coil provides similar parallel imaging capabilities.

Figure 6 (*bottom*) shows corresponding histograms formed from the 1/g-factor maps above, with histogram entries binned to 20 entries. For accelerations of R = 2 and R = 3, the 31-channel outperforms the 8-channel array with the majority of voxel distributions near 1/g = 1. Higher accelerations of R = 4 and R = 5 results in a complete loss of high 1/g factors for the 8-channel array, whereas the 31-channel array shows an improved performance with a similar 1/g-factor distribution to that of a conventional 32-channel array.

PET performance/attenuation of array coil

Figure 7 shows transverse slices of the CT images for each of the three coils at the center z = 0 and 7.5 cm from the center in each direction (z = ±7.5 cm). All slices lie within the PET FOV. The CT images show that there are more components on a standard 32-channel MR-only coil that would attenuate photons. The main absorbing components are densely packed

electrical components from the preamplifiers and highly attenuating cables, cable traps and cable plugs.

Figure 8 shows sinograms of attenuation correction factors (ACF) for the corresponding slices of the CT images shown in Figure 7, with the mean ACF displayed for the each slice ($z = 0$ and $z = \pm 7.5$ cm). At $z = 0$, the 31-channel PET/MR coil attenuates 12% more with respect to the 8-channel PET/MR coil, whereas the 32-channel MR-only coil attenuates 77% more. Similar results are obtained in both directions away from the center. The overall mean ACF for a total axial length of 20 cm, with 40 slices taken into account, spaced at 0.5 cm each is 1.13 for the 8-channel PET/MR coil, 1.33 for the 31-channel PET/MR coil and 2.40 for the 32-channel MR-only coil. Hence, we estimate that the 31-channel PET/MR coil attenuates 18% more on average and the 32-channel MR-only coil attenuates 112% times more, compared to the 8-channel PET/MR coil.

The artifact load of the 31-channel coil and the loss in photon counts due to the coil are demonstrated in Figure 9 with PET phantom data. Images from an [^{18}F]-solution-filled cylindrical phantom with the 8-channel or 31-channel coil in place are compared to a reference dataset without any coils present in the PET FOV. Normalized difference images relative to the reference image are shown next to the phantom images for each case. At the top in Figure 9, a maximum intensity projection of the attenuation map including the coils is shown and visualizes the amount of attenuation inside the PET FOV. Without accounting for attenuation correction of the coil (Figure 9, middle rows), artifacts and an overall loss in photon counts are visible. On average, the 8-channel and 31-channel coil show a 14% and 17% loss in photon counts, respectively. Based on this phantom data, the 31-channel coil attenuates 21% more on average than the 8-channel coil. In addition, an analysis based on 5 regions of interest (ROIs, shown in Figure 9, right) was carried out. Supporting Table S1 shows the loss in photon counts in terms of relative change for ROIs 1 to 5 in a plane at the center of the PET FOV. A plot of these ROIs over all planes along the length of the phantom is shown in Supporting Figure S2.

Attenuation correction was implemented for the 31-channel coil with an attenuation map created from CT scans. As a result, image artifacts were removed, so that the PET images are comparable to the reference image without any coil in the PET FOV (Figure 9, bottom rows). Moreover, attenuation due to the coil was largely accounted for, such that measured losses compared to the reference image reduced to 2% and 4% on average for the 8-channel and 31-channel coils, respectively. From an ROI-based analysis with ROIs 1 to 5, we found that ROIs at the center of the coil had the least relative change compared to the reference image and all ROIs showed a maximum of −5% change on average. The values for each ROI are listed in Table S1, and the values for all planes along the length of the phantom are shown in Figure S2.

Simultaneously acquired images from a healthy volunteer demonstrate the array's optimization towards obtaining highly sensitive PET/MR imaging data (Figure 10). The [^{18}F]FDG-PET data shows artifact-free images, reconstructed with respective coil attenuation maps. For MR images taken with the 31-channel coil, the higher SNR and lower

g-factor translate into improved image quality, as shown in the T1-weighted anatomical images (MEMPRAGE) with acceleration factors R=2 and R=4.

Discussion

Overall, the design of the PET-compatible array coil took into consideration three main design criteria: First, sensitivity improvement of the MR image compared to available coil designs for PET/MR systems; second, removal of all possible components (i.e. the preamplifiers) outside the PET FOV and third, the choice of coil components within the PET FOV for minimal attenuation of 511 keV photons while maintaining sensitivity from the MR signal.

The choice of electrical components within the PET FOV was a compromise between achieving the highest possible MR SNR and low attenuation/artifacts for the PET acquisition. Generally, electrical components that allow for high SNR are larger or contain more highly attenuating materials on circuit boards. But if the similar performance can be achieved with smaller components, those should be the preferred choice. It was thus necessary to evaluate all components for their properties before designing the coil. For example, thicker wires correspond to a higher quality factor in measurements and would be desirable, except for thicker wires causing more photon attenuation. As one tradeoff, we chose a thinner 18 awg copper wire for coil loops, contrary to previous coil designs, in which 26% thicker (16 awg) wires were used (8). Since the 18 awg wire loops only showed 6% less SNR, this was an acceptable tradeoff. Smaller wire loops showed much larger decreases in SNR and thus were not chosen. In coils with fewer receive channels, this may not have a large impact, but in the case of 31 or 32 channels, artifacts can become more pronounced. Hence, component choices and their arrangement should be taken into account during the coil design stage.

We evaluated the MR performance of the constructed 31-channel array with MR noise correlations, SNR maps and g-factor maps. We demonstrated superior MR performance of the 31-channel array over current existing arrays (an 8-channel receive array dedicated to the BrainPET scanner). At the same time, SNR and acceleration propertoes were not diminished in the 31-channel PET/MR coil compared to a 32-channel MR-only coil, even though we made somecompromises on the electrical components to reduce attenuation.

To assess the PET performance, we analyzed CT scans in sinogram space and determined attenuation correction factors at 511 keV. Moreover, we analyzed PET phantom data to compare the attenuation of the 31-channel coil to the existing 8-channel coil and a reference phantom without coils in the PET FOV. We showed that the constructed 31-channel PET/MR array has a similar attenuation to the 8-channel PET/MR array, even though it has nearly four times the number of channels. Additionally, the 31-channel array shows an improvement over conventional 32-channel coils in terms of attenuation properties. Thus the coil design can be seen as either improving MR performance at similar PET performance compared to the 8-channel PET-optimized array, or improving the PET performance at similar MR performance when compared to a 32-channel MR array.

Attenuation correction of PET images is a necessary processing step for accurate quantification of PET datasets. However, the implementation of attenuation corrections for MR coils is not straightforward: The geometry of the MR coil cannot be imaged since there are no transmission sources or CT available at PET/MR scanners that account for a reliable attenuation map before each scan. Prior knowledge of the attenuation map and its specific location is thus required. Therefore, it is desirable that components are fixed in a stable position to avoid relative movement of components that could partially invalidate attenuation maps acquired previously. To address this issue, the 31-channel coil was designed to fit tightly into the table bed and local transmit array because small displacements in space can lead to artifacts that can be challenging to correct for (13). Minimizing attenuation from MR coils during the design stage avoids unnecessary artifacts and increases true coincidences in PET images, leading to higher SNR.

While the conversion of Hounsfield units into linear attenuation coefficients via a bilinear transform is an established method for human tissues (24, 33), applying the same conversions on highly attenuating metals can introduce errors. Attenuation properties of coil components are usually not exactly known as extrapolation to 511 keV energies from CT scans is approximate. It is thus challenging to correct for all components accurately (13). On the CT images used for deriving attenuation maps, beam hardening artifacts often cause an overestimation of the Hounsfield units of highly attenuating electrical components (15). The standard conversion to linear attenuation coefficients we applied may thus overestimate the attenuation properties of the RF coil and it may result in overcorrection of the attenuation of the coil in PET images. While 511 keV transmission scans may provide a more accurate alternative to derive attenuation maps (16), the resolution of standard transmission images is too low for the high-resolution BrainPET camera employed here. In order to further improve the accuracy of attenuation evaluations and corrections, targeted conversion methods for non-tissue components and highly attenuating electronics need to be developed.

The design criteria for PET-compatible coils presented here are generally valid for multi-channel coils in PET/MR imaging. A similar, though slightly modified, design of the 31-channel coil presented here can be employed for the construction of 32-channel coils for newer-generation PET/MR scanners. New generation commercially available PET/MR scanners are targeted towards whole-body imaging, in which a longer PET FOV is present and automatic table movements allow for the acquisition of several bed positions in PET. In this case, preamplifiers would need to be moved an additional 5 cm further away from the coil to adjust to the PET FOV. Moreover, all preamplifiers should be moved to the superior end of the coil in order not to interfere with subsequent whole-body scans. Overall, the majority of design criteria can be employed as proposed in this work though.

The design of PET-compatible arrays is equally important for sequential PET/MR systems. In an integrated sequential scan setup, the subject and coils are generally not moved as the scan table switches position from one scanner to the other (35) to preserve the position of the patient. Hence, sequential PET/MR scanners face the same challenges from MR coil attenuation and specially designed coils are needed for such applications as well.

Conclusions

In this study, we presented design criteria for PET-compatible multichannel MR arrays and showed the design, construction and performance of a 31-channel receive array for human brain imaging that is optimized for simultaneous PET/MR imaging. The array is characterized by a sparse configuration of 511 keV absorptive materials in the PET FOV, placement of preamplifiers outside the PET FOV and a tight fit into a local transmit coil within a confined space of a BrainPET camera.

The 31-channel PET-compatible array coil enables higher sensitivity and better image quality for both PET and MRI. The superior performance of the 31-channel array was demonstrated with SNR and 1/g-factor maps in the MR domain, and with attenuation measurements of 511 keV absorptive materials in the PET domain. We successfully implemented accurate attenuation correction of the coil and demonstrated the coil performance with simultaneously acquired PET/MR brain images. Hence, this array coil enables new applications of high quality simultaneous PET and MR brain imaging in the clinic or research domain.

Supplementary Material

Refer to Web version on PubMed Central for supplementary material.

Acknowledgments

The authors thank Bastien Guerin, Jonathan Polimeni and Spencer Bowen for their help and contributions. This research was supported by grants from the National Institute of Health (R90DA023427, P41EB015896).

References

1. Catana C, Wu Y, Judenhofer MS, Qi J, Pichler BJ, Cherry SR. Simultaneous Acquisition of Multislice PET and MR Images: Initial Results with a MR-Compatible PET Scanner. J Nucl Med. 2006 Dec; 47(12):1968–1976. [PubMed: 17138739]
2. Schmand M, Burbar Z, Corbeil J, Zhang N, Michael C, Byars L, Eriksson L, Grazioso R, Martin M, Moor A, Camp J, Matschl V, Ladebeck R, Renz W, Fischer H, Jattke K, Schnur G, Rietsch N, Bendriem B, Heiss W-D. BrainPET: First human tomograph for simultaneous (functional) PET and MR imaging. Society of Nuclear Medicine Annual Meeting Abstracts. 2007 May.48(Supplement 2): 45P.
3. Catana C, Drzezga A, Heiss W-D, Rosen BR. PET/MRI for Neurologic Applications. J Nucl Med. 2012; 53:1916–1925. [PubMed: 23143086]
4. Sander CY, Hooker JM, Catana C, Normandin MD, Alpert NM, Knudsen GM, Vanduffel W, Rosen BR, Mandeville JB. Neurovascular coupling to D2/D3 dopamine receptor occupancy using simultaneous PET/functional MRI. PNAS. 2013:201220512.
5. Catana C, Procissi D, Wu Y, Judenhofer MS, Qi J, Pichler BJ, Jacobs RE, Cherry SR. Simultaneous in vivo positron emission tomography and magnetic resonance imaging. Proceedings of the National Academy of Sciences. 2008; 105(10):3705.
6. Wiggins GC, Triantafyllou C, Potthast A, Reykowski A, Nittka M, Wald LL. 32-channel 3 Tesla receive-only phased-array head coil with soccer-ball element geometry. Magnetic Resonance in Medicine. 2006 Jul; 56(1):216–223. [PubMed: 16767762]
7. Wiggins GC, Polimeni JR, Potthast A, Schmitt M, Alagappan V, Wald LL. 96-Channel receive-only head coil for 3 Tesla: Design optimization and evaluation. Magnetic Resonance in Medicine. 2009 Sep; 62(3):754–762. [PubMed: 19623621]

8. Keil B, Alagappan V, Mareyam A, McNab JA, Fujimoto K, Tountcheva V, Triantafyllou C, Dilks DD, Kanwisher N, Lin W, Grant PE, Wald LL. Size-optimized 32-channel brain arrays for 3 T pediatric imaging. Magnetic Resonance in Medicine. 2011 Dec; 66(6):1777–1787. [PubMed: 21656548]
9. Pruessmann KP, Weiger M, Scheidegger MB, Boesiger P. SENSE: sensitivity encoding for fast MRI. Magn Reson Med. 1999 Nov; 42(5):952–962. [PubMed: 10542355]
10. Griswold MA, Jakob PM, Heidemann RM, Nittka M, Jellus V, Wang J, Kiefer B, Haase A. Generalized autocalibrating partially parallel acquisitions (GRAPPA). Magnetic Resonance in Medicine. 2002 Jun; 47(6):1202–1210. [PubMed: 12111967]
11. Keil, B.; Biber, S.; Rehner, R.; Tountcheva, V.; Wohlfarth, K.; Hoecht, P.; Hamm, M.; Meyer, H.; Fischer, H.; Wald, LL. A 64-Channel Array Coil for 3T Head/Neck/C-spine Imaging; Proceedings of the International Society of Magnetic Resonance in Medicine, 19th annual meeting; 2011 May; p. 402
12. Tellmann L, Quick HH, Bockisch A, Herzog H, Beyer T. The effect of MR surface coils on PET quantification in whole-body PET/MR: Results from a pseudo-PET/MR phantom study. Medical Physics. 2011; 38(5):2795–2805. [PubMed: 21776816]
13. Catana C, van der Kouwe A, Benner T, Michel CJ, Hamm M, Fenchel M, Fischl B, Rosen B, Schmand M, Sorensen AG. Toward Implementing an MRI-Based PET Attenuation-Correction Method for Neurologic Studies on the MR-PET Brain Prototype. Journal of Nuclear Medicine. 2010 Sep; 51(9):1431–1438. [PubMed: 20810759]
14. Paulus DH, Braun H, Aklan B, Quick HH. Simultaneous PET/MR imaging: MR-based attenuation correction of local radiofrequency surface coils. Medical Physics. 2012; 39:4306–4315. [PubMed: 22830764]
15. Paulus DH, Tellmann L, Quick HH. Towards improved hardware component attenuation correction in PET/MR hybrid imaging. Phys Med Biol. 2013; 58:8021. [PubMed: 24168832]
16. MacDonald LR, Kohlmyer S, Liu C, Lewellen TK, Kinahan PE. Effects of MR surface coils on PET quantification. Med Phys. 2011; 38:2948–2956. [PubMed: 21815368]
17. Sander CY. Design Criteria of an MR-PET Array Coil for Highly Parallel MR Brain Imaging. Proc Intl Soc Mag Reson Med. 2011; 19:0169.
18. Judenhofer MS, Wehrl HF, Newport DF, Catana C, Siegel SB, Becker M, Thielscher A, Kneilling M, Lichy MP, Eichner M, Klingel K, Reischl G, Widmaier S, Röcken M, Nutt RE, Machulla H-J, Uludag K, Cherry SR, Claussen CD, Pichler BJ. Simultaneous PET-MRI: a new approach for functional and morphological imaging. Nature Medicine. 2008 Mar; 14(4):459–465.
19. Howseman AM, Bowtell RW. Functional magnetic resonance imaging: imaging techniques and contrast mechanisms. Philos Trans R Soc Lond B Biol Sci. 1999 Jul; 354(1387):1179–1194. [PubMed: 10466145]
20. Golay X, Jiang H, van Zijl PCM, Mori S. High-resolution isotropic 3D diffusion tensor imaging of the human brain. Magnetic Resonance in Medicine. 2002 May; 47(5):837–843. [PubMed: 11979561]
21. Phelps ME. Positron Emission Tomography Provides Molecular Imaging of Biological Processes. PNAS. 2000 Aug; 97(16):9226–9233. [PubMed: 10922074]
22. Rieke V, Ganguly A, Daniel BL, Scott G, Pauly JM, Fahrig R, Pelc NJ, Butts K. X-ray compatible radiofrequency coil for magnetic resonance imaging. Magnetic Resonance in Medicine. 2005 Jun; 53(6):1409–1414. [PubMed: 15906285]
23. Possanzini, C.; Boutelje, M. Influence of magnetic field on preamplifiers using GaAs FET technology; Proceedings of the 16th Annual Meeting of ISMRM; Toronto, Canada. 2008; p. 1123
24. Burger C, Goerres G, Schoenes S, Buck A, Lonn A, Von Schulthess G. PET attenuation coefficients from CT images: experimental evaluation of the transformation of CT into PET 511-keV attenuation coefficients. European journal of nuclear medicine and molecular imaging. 2002; 29(7):922–927. [PubMed: 12111133]
25. Byars LG, Sibomana M, Burbar Z, Jones J, Panin V, Barker WC, Liow J-S, Carson RE, Michel C. Variance reduction on randoms from coincidence histograms for the HRRT. 2005 IEEE Nuclear Science Symposium Conference Record. 2005; 5:2622–2626.

26. Watson CC. New, faster, image-based scatter correction for 3D PET. 1999 IEEE Nuclear Science Symposium, 1999, Conference Record. 1999; 3:1637–1641. vol.3.

27. Chonde DB, Abolmaali N, Arabasz G, Guimaraes AR, Catana C. Effect of MRI Acoustic Noise on Cerebral Fludeoxyglucose Uptake in Simultaneous MR-PET Imaging. Investigative Radiology. 2013; 48:302–312. [PubMed: 23462677]

28. Hubbell J. Photon mass attenuation and energy-absorption coefficients. The International Journal of Applied Radiation and Isotopes. 1982; 33(11):1269–1290.

29. Roemer PB, Edelstein WA, Hayes CE, Souza SP, Mueller OM. The NMR phased array. Magnetic Resonance in Medicine. 1990 Nov; 16(2):192–225. [PubMed: 2266841]

30. Reykowski A, Wright SM, Porter JR. Design of Matching Networks for Low Noise Preamplifiers. Magnetic Resonance in Medicine. 1995 Jun; 33(6):848–852. [PubMed: 7651124]

31. Kellman P, McVeigh ER. Image reconstruction in SNR units: a general method for SNR measurement. Magn Reson Med. 2005 Dec; 54(6):1439–1447. [PubMed: 16261576]

32. Van der Kouwe AJW, Benner T, Salat DH, Fischl B. Brain morphometry with multiecho MPRAGE. NeuroImage. 2008; 40:559–569. [PubMed: 18242102]

33. Izquierdo-Garcia D, Chen KT, Hansen AE, Förster S, Benoit D, Schachoff S, Fürst S, Chonde DB, Catana C. New SPM8-based MRAC method for simultaneous PET/MR brain images: comparison with state-of-the-art non-rigid registration methods. PSMR. 2014 #72, Greece.

34. Carney JPJ, Townsend DW, Rappoport V, Bendriem B. Method for transforming CT images for attenuation correction in PET/CT imaging. Medical Physics. 2006; 33:976–983. [PubMed: 16696474]

35. Zhang, B.; Pal, D.; Hu, Z.; Ojha, N.; Guo, T.; Muswick, G.; Tung, C.; Kaste, J. Attenuation correction for MR table and coils for a sequential PET/MR system; Nuclear Science Symposium Conference Record (NSS/MIC), 2009 IEEE; 2009. p. 3303-3306.

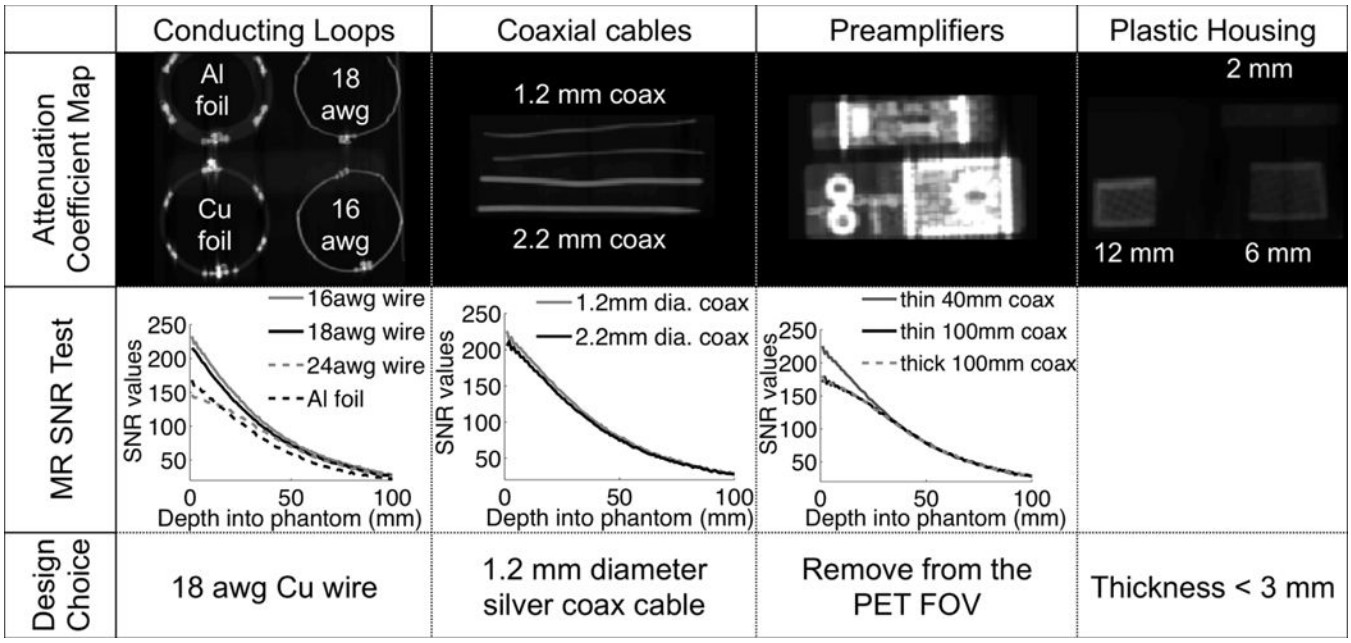

Figure 1.

511 keV attenuation map of coil components evaluated for the design of the 31-channel PET/MR array coil (1st row), showing high attenuation of the preamplifiers and thick metal or plastic components. Each electrical component was tested for its MR SNR in a single-loop configuration on a water phantom (2nd row). The final design choices reflect the goal to reduce attenuation but preserve SNR for MRI (3rd row).

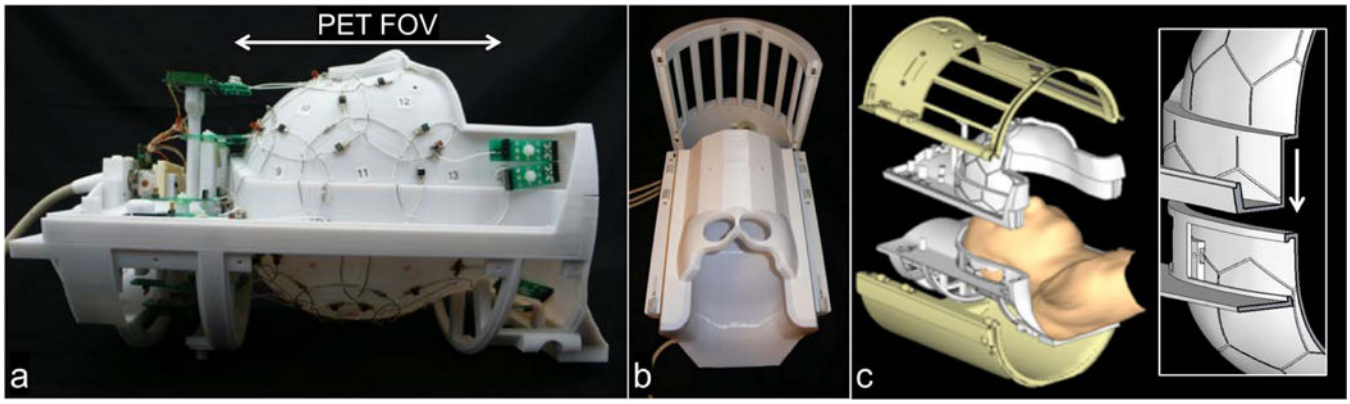

Figure 2.

The 31-channel PET/MR array coil is divided into an anterior and posterior part, with 15 and 16 channels respectively. (a) Side view of the array, with overlapping loop design and preamplifiers outside the FOV of the PET camera. (b) Fit of the receive coil with cover into the local transmit coil. (c) CAD design of the coil with an anterior and posterior part and a magnification of the mechanical rim system that allows for an overlapped loop design between the two coil parts.

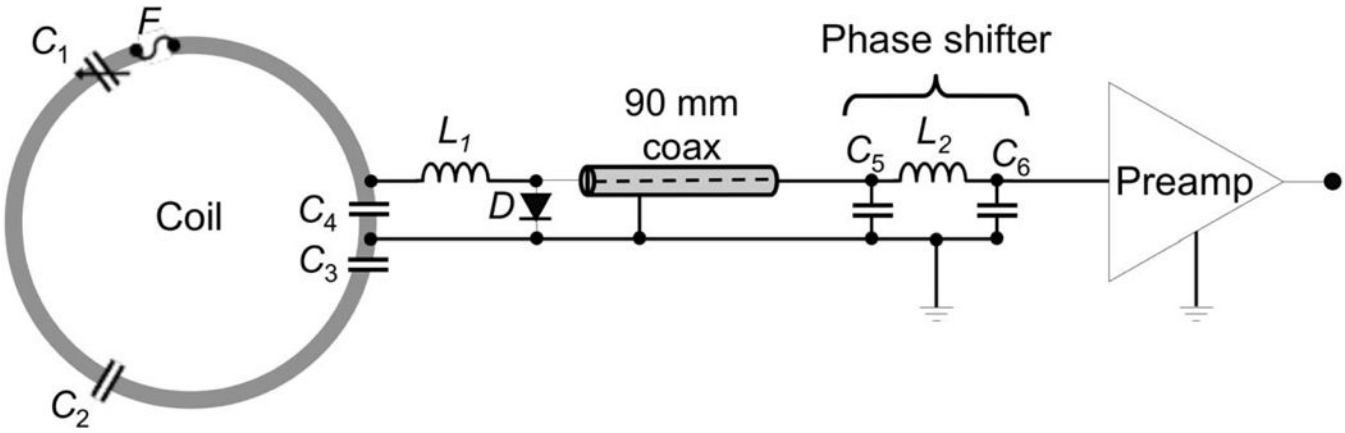

Figure 3.

Circuit schematic for coil elements with a long coaxial cable that allows placement of the preamplifier outside the PET FOV. In order to maintain a λ/2 phase shift, a pi phase shifter is located before the preamplifier chain.

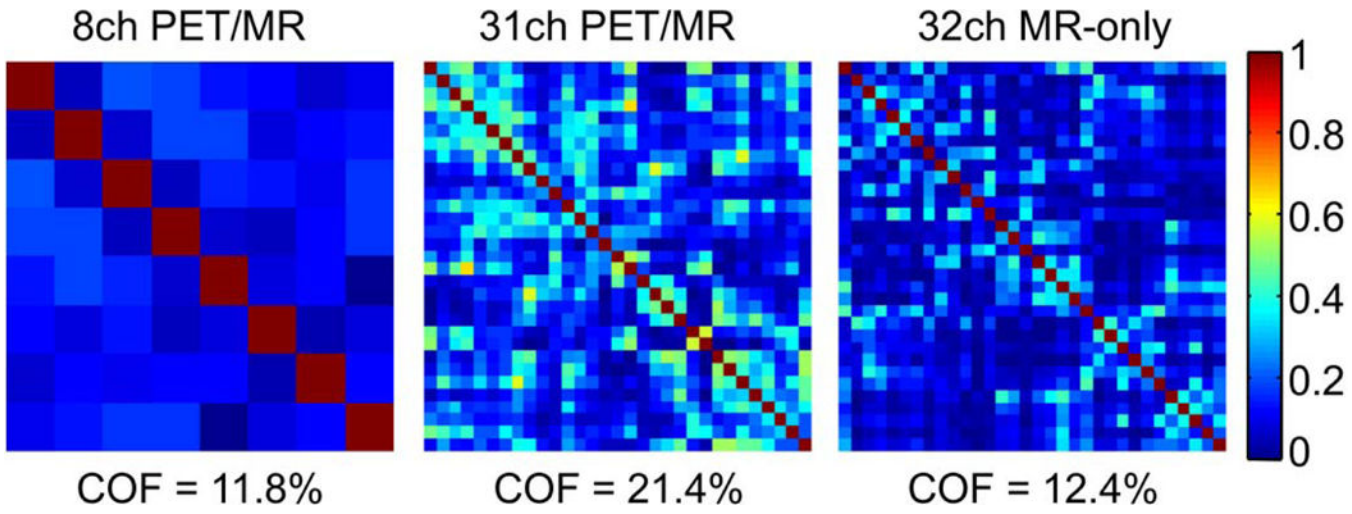

Figure 4.

Noise correlation matrices for the 8-channel PET/MR, the 31-channel PET/MR and the 32-channel MR-only array. The average noise correlation is 11.8%, 21.4% and 12.4% respectively.

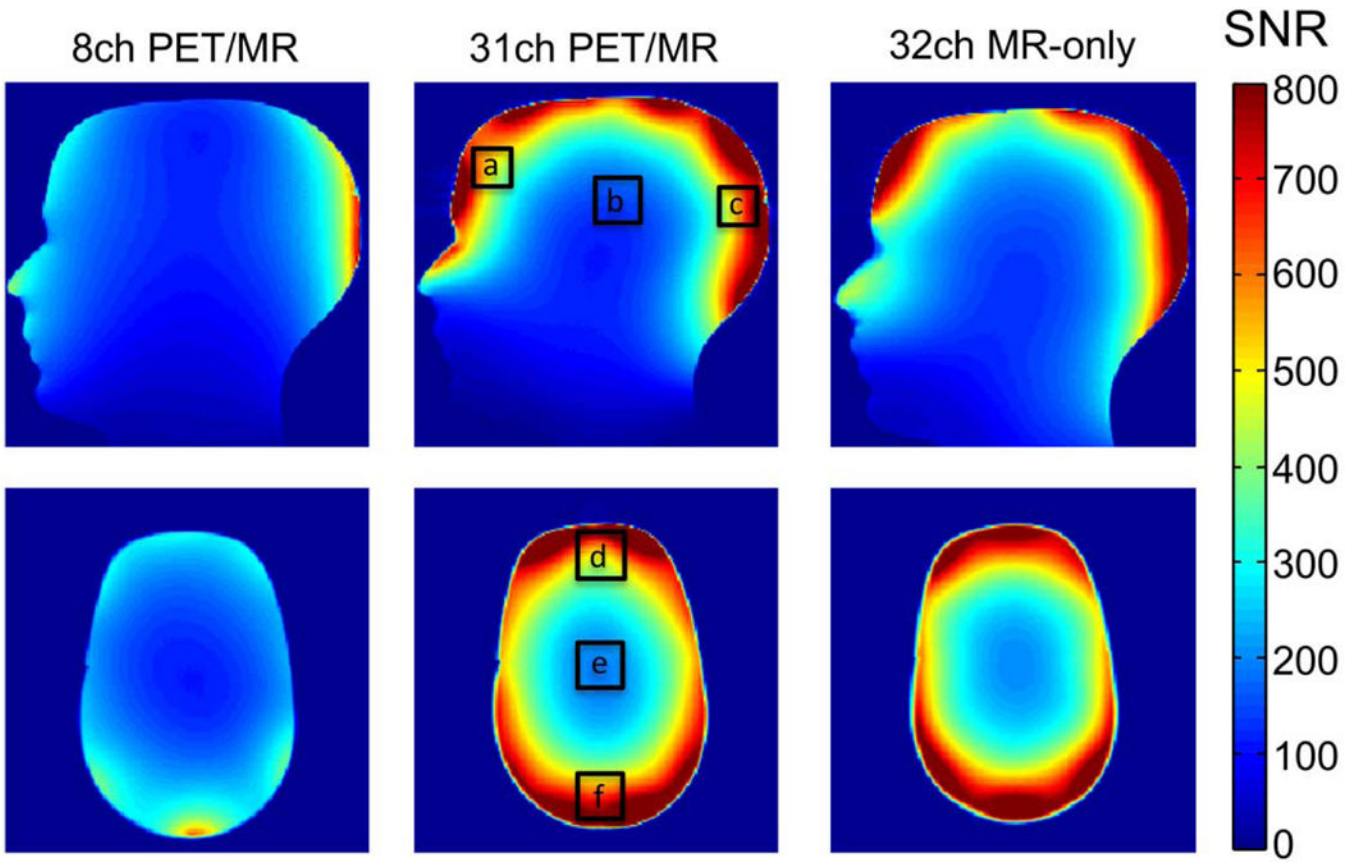

Figure 5.

Signal to noise maps of a human head-shaped water phantom (sagittal and axial slice) for the 8-channel PET/MR, the 31-channel PET/MR and a standard 32-channel MR-only array. The gain in SNR compared to the 8ch PET/MR coil for the ROIs shown is: (a) 2.3, (b) 1.6, (c) 1.7, (d) 2.2, (e) 1.8, (f) 2.1. The SNR of the 31-channel PET/MR coil shows a large improvement compared to the 8-channel coil, and shows no overall SNR loss compared to the 32-channel MR-only array.

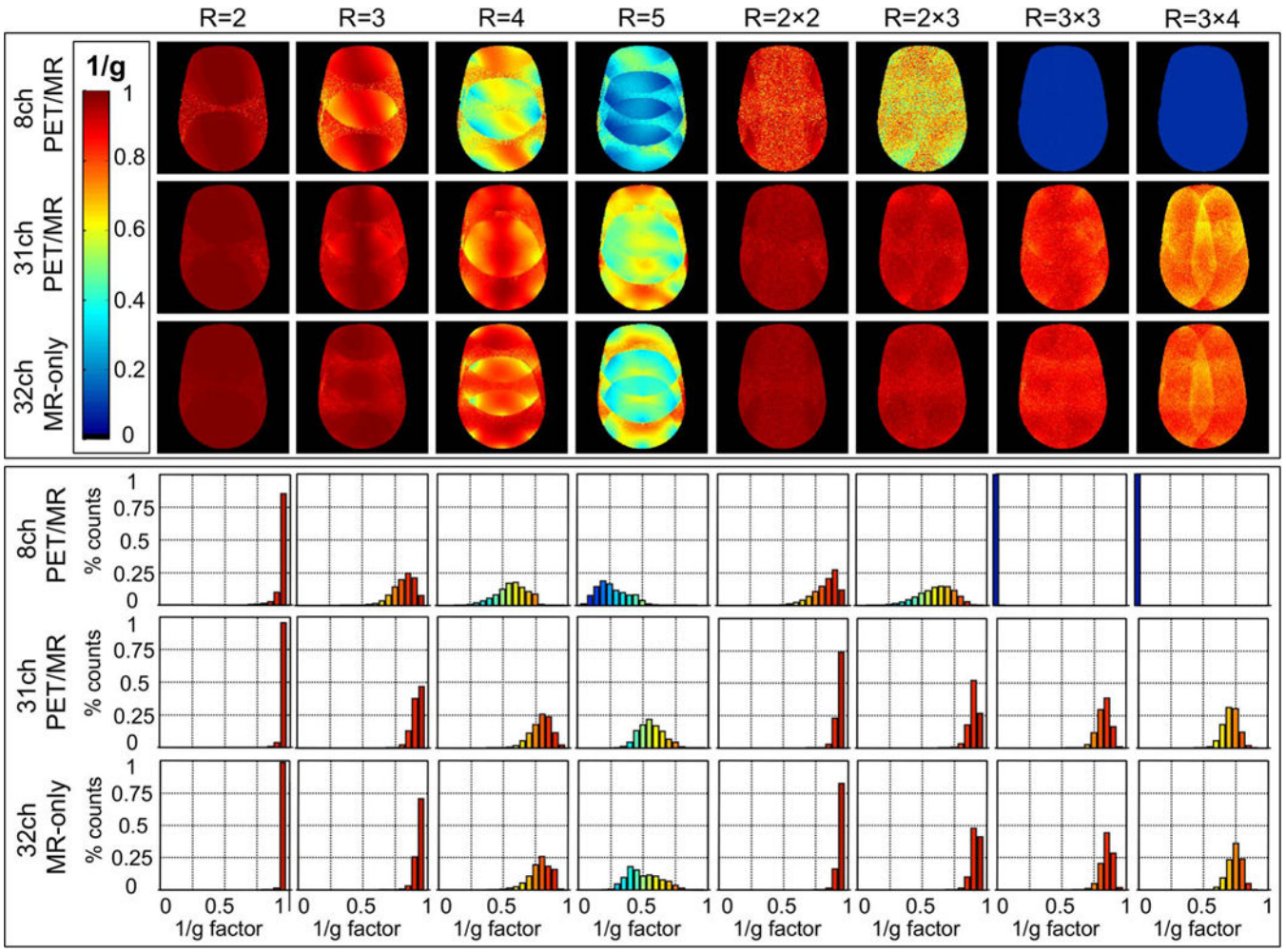

Figure 6.

Top: 1/g factor maps for the 8-channel PET/MR, the 31-channel PET/MR and the 32-channel MR-only array for acceleration factors R in 1D and 2D. *Bottom:* Corresponding histograms of 1/g factor maps for the three coils in comparison. Compared to the 8-channel PET/MR coil, the 31-channel PET/MR coil shows much higher 1/g factors values at all acceleration stages. Despite the design constraints for PET compatibility, the 31-channel PET-optimized array performs similarly to an MR-only array with an equivalent number of channels.

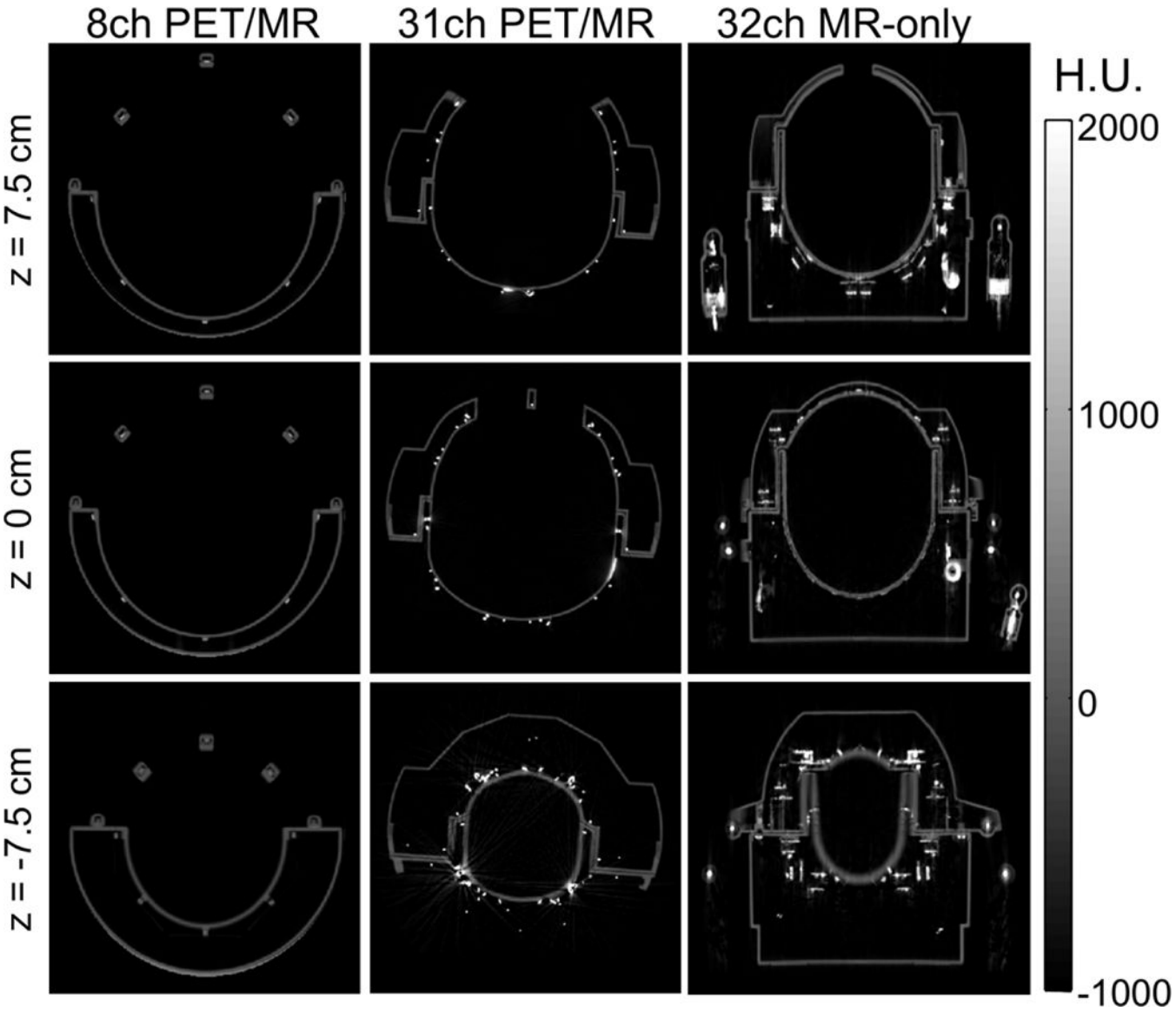

Figure 7.

Axial CT scans for z-positions −7.5 cm, 0 cm and 7.5 cm of the 8-channel PET/MR, the 31-channel PET/MR and a standard MR-only 32-channel coil. While the 8-channel coil shows the least material in the PET FOV, the 32-channel MR-only coil shows attenuating coil components, such as the plugs, preamplifiers and cable traps. Compared to these two coils, the 31-channel PET/MR coil shows more metal due to the higher number of coils but does not have large attenuating coil components in the PET FOV.

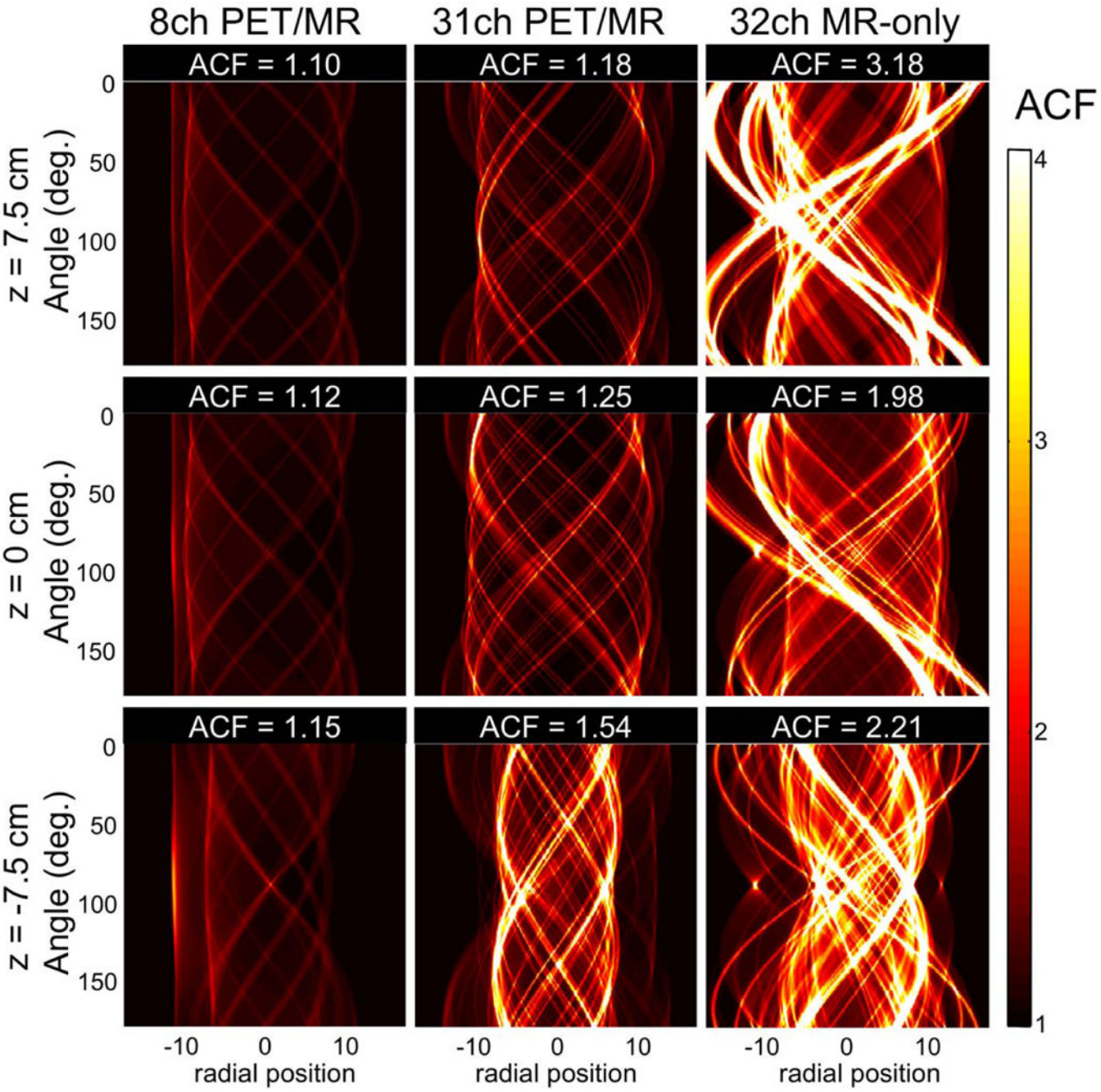

Figure 8.

Sinograms calculated from a forward projection of the CT scans (shown in Figure 7) for z-positions −7.5 cm, 0 cm and 7.5 cm. The mean attenuation correction factors (ACF) of the 31-channel PET/MR coil, the 8-channel PET/MR and a standard MR-only 32-channel coil are shown for each slice. This estimation shows that while the 31-channel PET/MR would only attenuate between 18–54% of the 511 keV photons (similar to the 8-channel PET/MR coil), an MR-only standard 32-channel coil would attenuate much more photons (up to 218%).

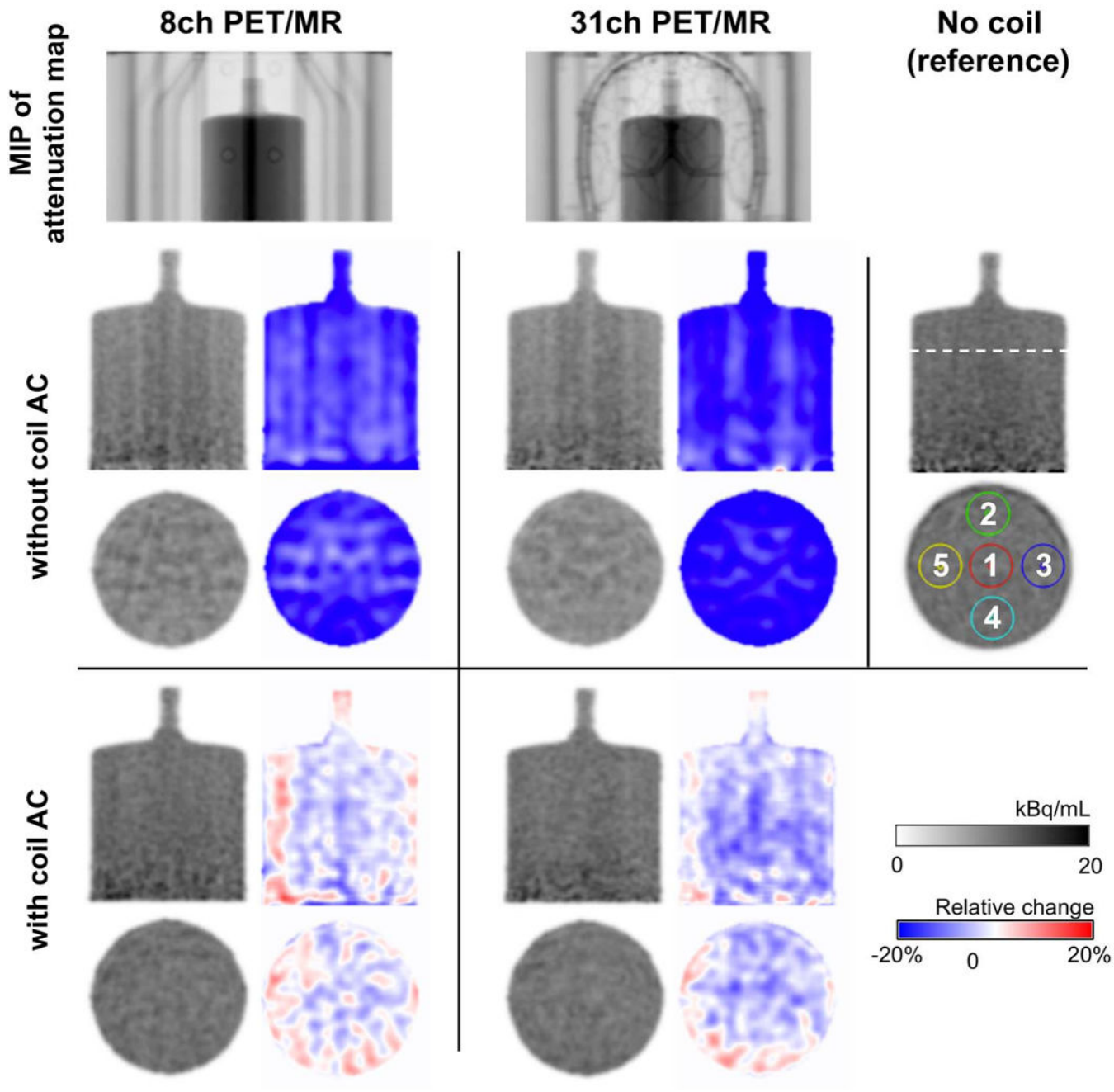

Figure 9.

PET images (in gray-scale) of a cylindrical phantom filled with [^{18}F]-solution acquired using the setup with the 8-channel (left), 31-channel (center) or no coil as reference (*right*); and corresponding images of relative change (blue-red scale) in percent (with respect to the reference image with no coils). *Top row:* A maximum intensity projection (MIP) of the attenuation map shows the location of the phantom in the coil and the materials inside the PET FOV. *Middle rows*: Coronal and transaxial slices of the phantom for each setup without coil attenuation correction (AC) applied. Images show artifacts and loss in photon counts, compared to the reference image without coils in the PET FOV. *Bottom rows:* Coronal and

transaxial slices of the phantom with attenuation correction of the coils implemented, in which images do not display any artifacts.

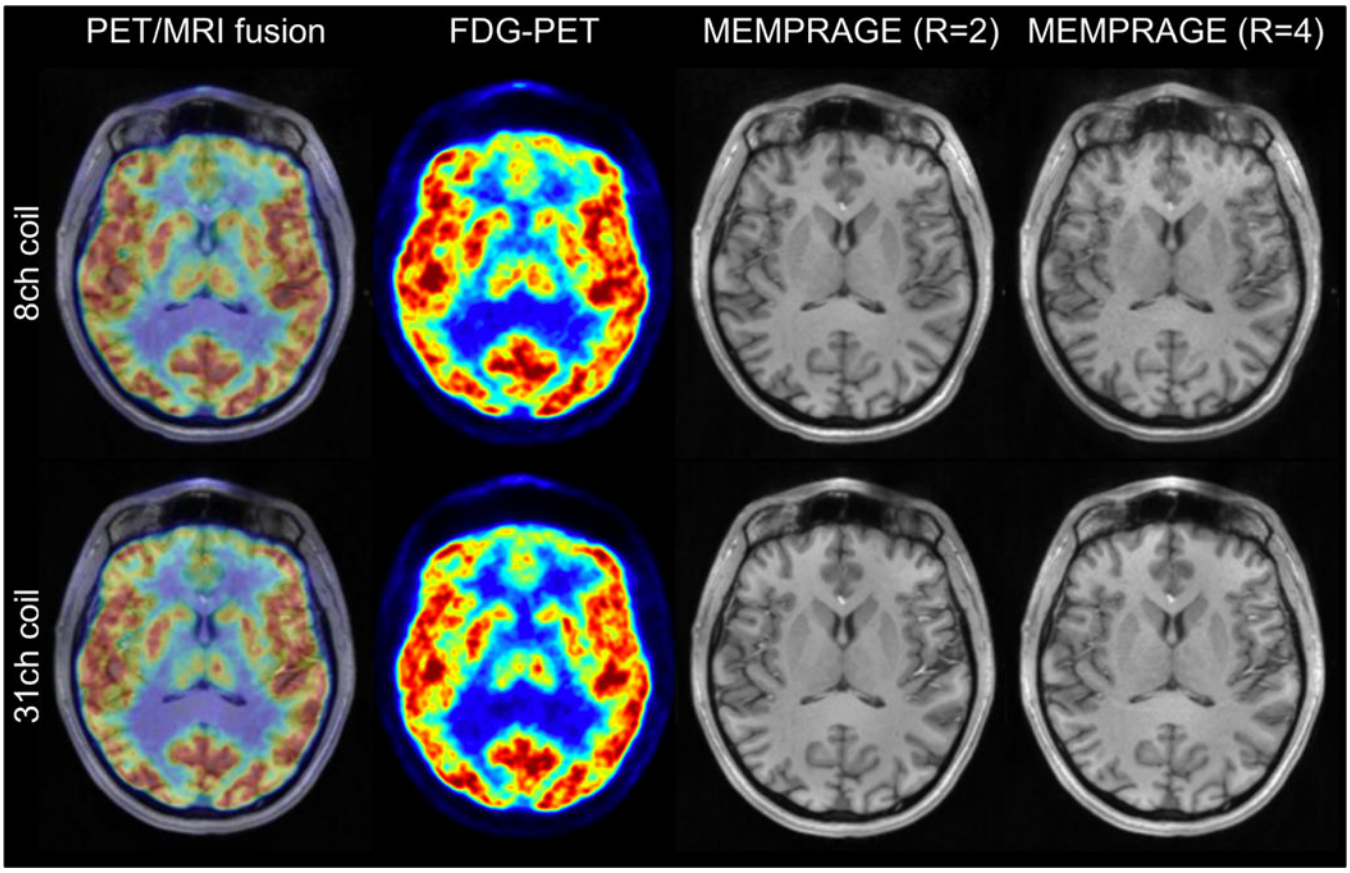

Figure 10.

Simultaneously acquired PET ([^{18}F]FDG) and MRI in a human subject shown as a fused image (*left*). Artifact-free PET images (*left center*) demonstrate an accurate implementation of the 31-channel coil attenuation correction. MR images obtained with the 8-channel and 31-channel coil show T1 anatomy (MEMPRAGE at acceleration R=2 (*center right*) and R=4 (*right*)) and the superior g-factor and SNR of the 31-channel coil.